

Permeability and elastic properties of rocks from the northern Hikurangi margin: Implications for slow-slip events

Nicola Tisato¹, Carolyn Bland¹, Harm Van Avendonk¹, Nathan Bangs¹, Omar Alamoudi¹, Kelly Olsen¹, and Andrew Gase¹

¹Affiliation not available

January 24, 2023

Abstract

Fluid flow and pore-pressure cycling are often invoked as controls to slow slip events (SSEs), such as those that frequently occur at the northern Hikurangi margin (HM) of New Zealand. To better understand fluid flow in the forearc system, we examined the relationship between elastic properties, compaction, porosity, and permeability of Cretaceous to Pliocene mudstones from the Raukumara peninsula. We found that the permeability of the deep wedge is too low to drain fluids, but fracturing increases permeability by orders of magnitude, making fracturing key for fluid flow. In weeks to months, plastic deformation and clay swelling heal the fractures restoring the initial permeability. We conclude that overpressures at the northern HM might partly dissipate during SSEs due to enhanced permeability near faults. However, in the weeks to months following an SSE, healing in the prism will lower permeability, forcing pore pressure to rise and a new SSE to occur.

Nicola Tisato¹, Carolyn D. Bland^{1*}, Harm Van Avendonk², Nathan Bangs², Omar Alamoudi¹, Kelly Olsen²⁺, Andrew Gase²⁺⁺

¹ Department of Geological Science, Jackson School of Geosciences, The University of Texas at Austin – U.S.

³ Institute for Geophysics, Jackson School of Geosciences, The University of Texas at Austin, U.S.

* Now at: Pariveda Solutions, Dallas Texas, U.S.

+ Now at: .

++ Now at: Department of Geology, Western Washington University, Bellingham WA.

Corresponding author: Nicola Tisato (nicola.tisato@jsg.utexas.edu)

Key Points:

- Elastic properties, plastic deformation, and permeability of Hikurangi margin rocks
- Permeability-porosity relationship in accretionary prisms
- Clay swelling and plastic deformation controls permeability healing, providing a mechanism justifying slow-slip event cyclicity

Abstract

Fluid flow and pore-pressure cycling are often invoked as controls to slow slip events (SSEs), such as those that frequently occur at the northern Hikurangi margin (HM) of New Zealand. To better understand fluid flow in the forearc system, we examined the relationship between elastic properties, compaction, porosity, and permeability of Cretaceous to Pliocene mudstones from the Raukumara peninsula. We found that the permeability of the deep wedge is too low to drain fluids, but fracturing increases permeability by orders of

magnitude, making fracturing key for fluid flow. In weeks to months, plastic deformation and clay swelling heal the fractures restoring the initial permeability. We conclude that overpressures at the northern HM might partly dissipate during SSEs due to enhanced permeability near faults. However, in the weeks to months following an SSE, healing in the prism will lower permeability, forcing pore pressure to rise and a new SSE to occur.

Plain Language Summary

Earth's crust is composed of many tectonic plates fitting together like jigsaw puzzle pieces. Along active converging margins, where tectonic plates subduct in the mantle, the forces driving the plate convergence can trigger large earthquakes. However, these subduction zones often deform without producing earthquakes, but through slow-slip. The Hikurangi Margin (HM) of New Zealand is a well-studied subduction zone, producing both earthquakes and slow-slip events. The northern HM exhibits more frequent and shallower slow-slip events than the southern margin. Understanding what controls such differences can help improve the general understanding of subduction zone fault mechanics and earthquakes. One of the hypotheses is that the differences between the deformation of the northern and southern HM are controlled by the pore pressure at depth. We tested the elastic and fluid-transport properties of four samples from the northern HM and found that the overriding plate, if not fractured, would be impermeable to fluids. We also tested a fractured sample and observed efficient healing that resets the initial permeability. We conclude that fracturing the overriding plate is fundamental to draining the fluids carried at depth by the subducting plate, and slow-slip may control fracturing creating new pathways for fluids to escape to the seafloor.

1 Introduction

At the shallow (<15 km depth) portion of the plate interface of subduction zones, scientists have found that convergence between the tectonic plates is often accommodated by modes of slip in between fast earthquakes and aseismic creep (Saffer & Wallace, 2015). Slow-slip events (SSEs) represent one class of such transient phenomena, which can lead to several centimeters of slip over several days to months (Schwartz & Rokosky, 2007). The relatively large seismic moment released by shallow SSEs, comparable to that of earthquakes (Passarelli et al., 2021), proves important to understand these events and how they influence the seismogenic character of a convergent margin. Specific frictional properties and stress heterogeneities along the plate interface might favor SSEs (Barnes et al., 2020; Bell et al., 2010; Im et al., 2020; Rabinowitz et al., 2018). However, since the subducting oceanic crust and sediments release large volumes of seawater, it is also apparent that elevated fluid pressures periodically lower the effective stress on the shallow megathrust or splay faults, which may support SSEs (Warren-Smith et al., 2019).

The northern Hikurangi margin (HM) of North Island, New Zealand, is a subduction zone with a shallow forearc and plate interface, where sediment accretion, compaction, and deformation have been modulated for millions of years by underthrusting seamounts (Gase et al., 2021; Sun et al., 2020) (Fig. S1). Subducting topography (e.g., seamounts) may cause stress heterogeneities (Leah et al., 2022; Sun et al., 2020) and fluid pressure transients (Shaddox & Schwartz, 2019) that can lead to SSEs, several of which have been characterized in great detail by onshore geodetic and offshore absolute pressure gauge (APG) data (Yohler et al., 2019). Offshore Gisborne SSEs occur every 1-2 years and can last for several weeks, during which 5 to 30 cm of slip may be accommodated (Wallace, 2020). Temporal variations in the character of earthquake focal mechanisms within the subducting oceanic crust provide compelling evidence for low effective stress before an SSE (Warren-Smith et al., 2019). This observation suggests that the increase in fluid pressure enables SSEs and that the slip itself is accompanied by fluid release. Nevertheless, fluid transport through the accretionary wedge in this deformation cycle is not yet well understood.

The physical properties of accreted sediments of the northern HM and their relationship to slip phenomena have been studied recently with the use of cores and data from the 2018 IODP expedition 372/375 (Wallace et al., 2019). The resulting studies have shed new light on the frictional properties, shallow dewatering, and faulting near the seafloor (Aretusini et al., 2021; Dutilleul et al., 2021; Fagereng et al., 2019; French & Morgan, 2020; Shreedharan et al., 2022). However, to understand how fluid-flow and deformation interplay

in the deeper prism, we also consider the physical properties of older, compacted and diagenetically mature strata (Bland et al., 2015). Here we present and discuss laboratory testing performed on rock samples from the subaerial northern HM as proxies of deep rocks in the prism to better understand fluid transport within the subduction zone.

2 Materials and Method

To test the compaction, elastic, and transport properties of rocks from the northern HM, we collected samples from outcrops on the Raukumara peninsula in February 2019 (Fig. S1) representing the backstop and portions of the accretionary wedge that experienced different degrees of diagenesis (Fig. 1). In the central part of the peninsula, we collected a meta-greywacke from the Jurassic Torlesse terrane forming the backstop for the accretionary wedge (sample MO02) (Adams & Graham, 1996; Mortimer et al., 2014). Just east of the Torlesse terrane, we sampled a glauconitic mudstone from the Late Cretaceous to Paleocene Tinui Group (sample MT07) that likely represents an early passive margin deposit, now deeply buried in the accretionary wedge (Mortimer et al., 2014). Closer to the East coast, we collected samples GB13 and FB12, mudstones representative of the middle Miocene Tolaga Group, which was deposited in slope basins after subduction initiated along the HM (van de Lagemaat et al., 2022), and the Pliocene Mangaheia Group, respectively.

We determined mineral abundances and assemblages of each sample through X-ray diffraction (XRD) analyses (Fig. 1) and transmitted light microscopy by preparing transparent 30 μm in thickness thin-sections. To estimate density, porosity, compressional (P) and shear (S) ultrasonic wave velocities, and helium gas permeability, we prepared cylindrical core plugs with parallel end faces for each sample (Fig. 1, see supporting information). Samples were tested at the UT Austin Rock-Deformation-Laboratory for confining pressures (P_c) up to 200 MPa (~ 12.5 km depth for hydrostatic pore pressure and overburden density of 2.6 g/cm^3), and deviatoric vertical force (F_v) ~ 2.6 kN. Each core plug was mounted inside a PVC jacket and between two core holders equipped with ultrasonic transducers and fluid ports allowing to saturate the core and measure its permeability. This sample assembly is mounted inside the triaxial cell (NER Autolab 1500) between the load cell and the vertical force piston. We define the mean stress as $\sigma_M = \frac{\sigma_1 + \sigma_2 + \sigma_3}{3}$, where $\sigma_2 = \sigma_3 = P_c$ and σ_1 is the maximum vertical stress: $\sigma_1 = \sigma_d + P_c$, where $\sigma_d = \frac{F_v}{A}$ is the deviatoric stress and A is the sectional area of the core plug. We also define effective stress (σ') as the difference between the mean stress and the pore pressure: $\sigma' = \sigma_M - P_p$.

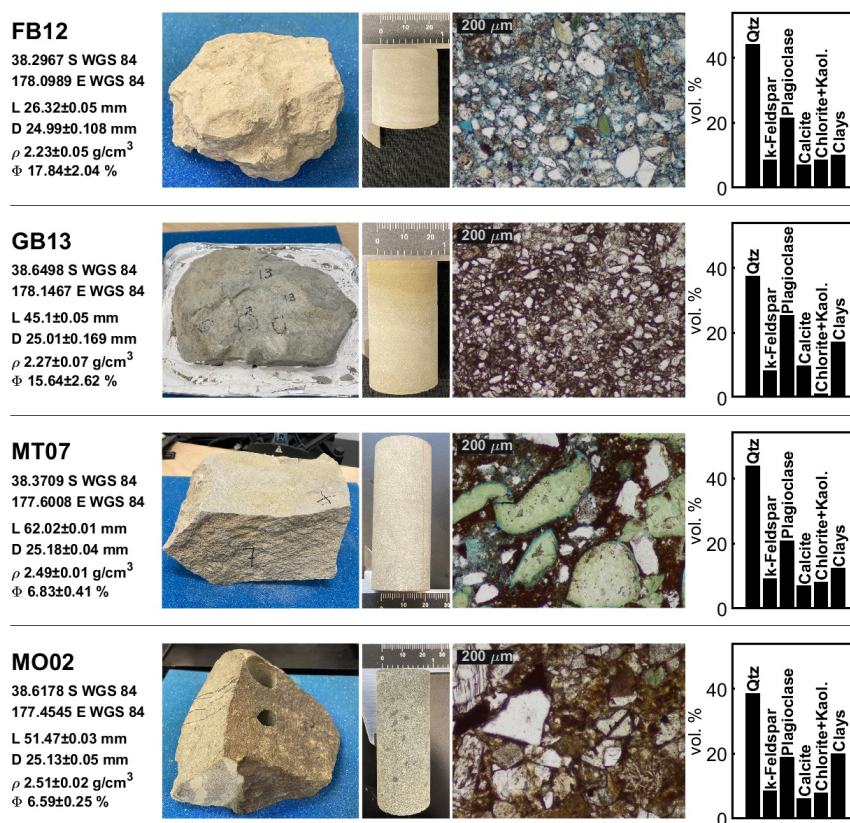
We measured ultrasonic velocities using the transmission method at room temperature and a frequency of ~ 800 kHz (Birch, 1960). To understand the effect of saturation on the ultrasonic velocities, we measured the ultrasonic velocities of sample GB13 saturated with water previously chemically equilibrated with the sample. During 30 hours, we recorded the injection of 4.7 ml of this aqueous fluid, equivalent to 136% of sample GB13 pore space volume (see supporting information).

Sample permeabilities were calculated through the transient method measuring the pressure equilibration of the helium gas contained in two volumes connected to the sample end-faces and flowing through the sample (Sutherland & Cave, 1980) (see supporting information). To understand the effect of porosity reduction on the permeability of young, loosely consolidated rocks, we measured FB12 permeability before and after mechanical compaction, which was assumed to be isotropic. After we measured ultrasonic velocities and permeabilities at confining pressures up to 70 MPa, while maintaining a constant σ_d to 5 MPa, we increased P_c stepwise to 100, 150 and 200 MPa and waited for 19, 24 and 5 hours to measure creep until the observed shortening rate was less than 1 $\mu\text{m}/\text{hour}$. Finally, we measured the sample permeability for varying confining pressures up to 200 MPa.

To study the influence of fracturing on HM rocks permeability, we fractured sample MT07 through a Brazilian test, causing the vertical splitting of the sample along a sub-vertical fracture connecting the opposite end-faces of the core plug. Then, we performed two sets of permeability tests and collected three micro-computed tomographies (μCT) at different times S1-S3, to seek evidence of temporal variations in permeability and fracture aperture. At day 1 we fractured the sample and collected S1. Between day 2 and 9 we conducted

the set of permeability tests kT1 at σ_m ranging 24 to 65 MPa. During kT1 (day 3 to 5) we promoted healing by keeping the sample at a confining pressure of 70 MPa. After kT1 and for the next 39 days, the sample remained inside the pressure vessel with negligible confinement and normal stress applied. Between day 48 and day 77 we conducted the set of permeability tests kT2 at σ_m ranging 5.6 to 64 MPa. S2 was acquired after kT2. Then, the jacketed sample was placed in a humidity-controlled chamber equipped with a water container and a thermo-hygrometer. For 72 hours, a medium to low vacuum (<0.5 bar) was maintained to promote water evaporation, causing the chamber relative humidity to remain above 97%. Exposing the fracture surfaces to moisture likely activating clays such as smectites with pronounced swelling properties (Villar et al., 2005). Finally, we acquired S3 and a thin section perpendicular to the sample axis was produced from the fractured sample. On the thin section, we examined the morphology of the fracture for evidence of clay infilling, possibly caused by plastic deformation and triggered by clay swelling (see supporting information).

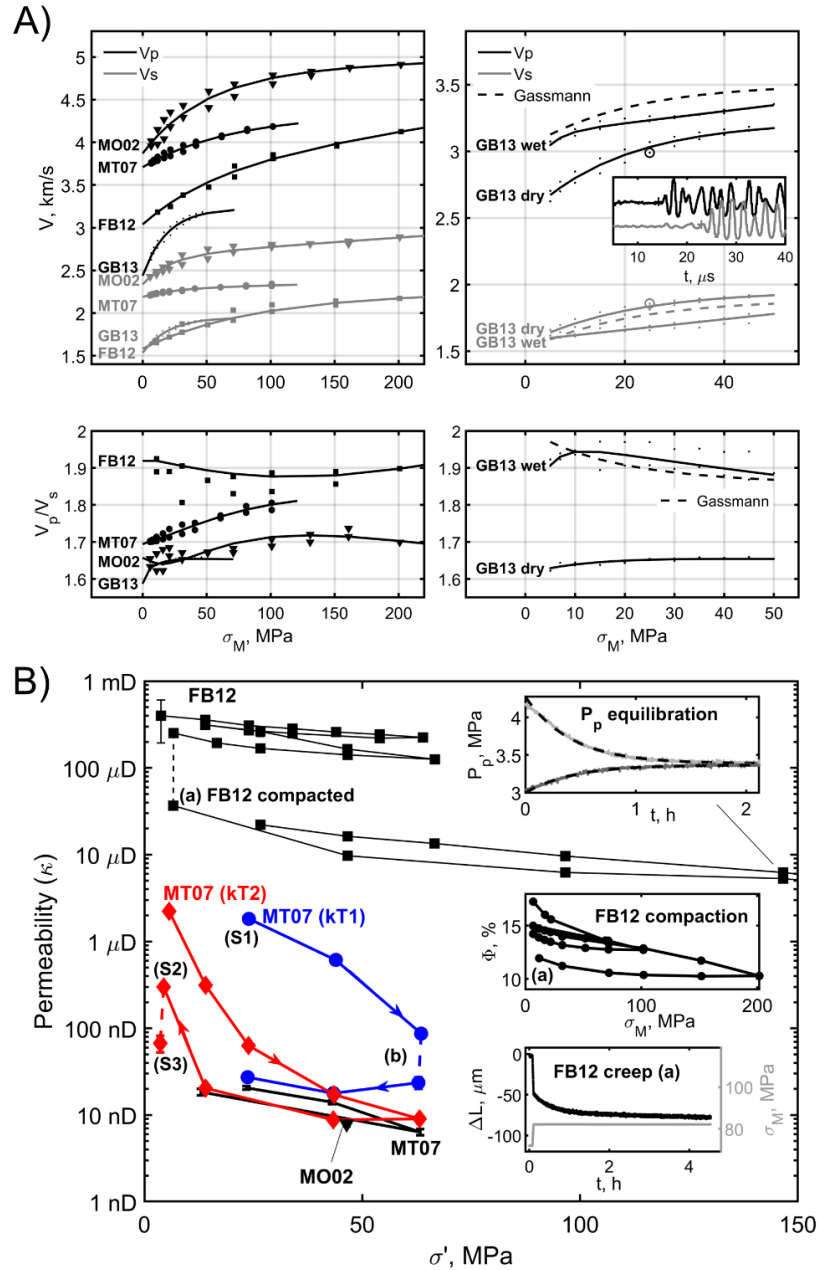
CT scans were acquired at $33.3 \mu\text{m}$ per voxel resolution using an NSI scanner. Each μCT dataset comprises 1600 16-bits TIFF images perpendicular to the sample axis recording the entire sample except 4.37 mm at the top and bottom of the sample. After normalization and segmentation, we calculated fracture apertures (B) for each CT dataset by producing fracture aperture distribution projections (FADP) whose mean and standard deviation provided average apertures (B_m) and associated uncertainties (see supporting information).



3 Results

Figure 1. For each sample, the left column reports the geographic coordinates, length (L), diameter (D), density (ρ), and porosity (Φ). The three center columns are pictures of hand samples and transmitted light microphotographs. The right column reports mineral compositions according to X-ray diffraction analyses (XRD).

The four samples are mudstones containing more than 60% quartz and feldspars. The remaining minerals are calcite, chlorite, and clays representing at least 20% of the total volume. Resource limitations impeded us from separating the abundances of micas and illite-smectite clay minerals. Porosities vary between 7 and 18%, where the tighter samples (MT07 and MO02) have a longer diagenetic or metamorphic history. Microphotography reveals that the grain size varies significantly among the four samples: Sample GB13 has the smallest grain size (<20 μm), while MT07 presents the largest grain size (<300 μm).



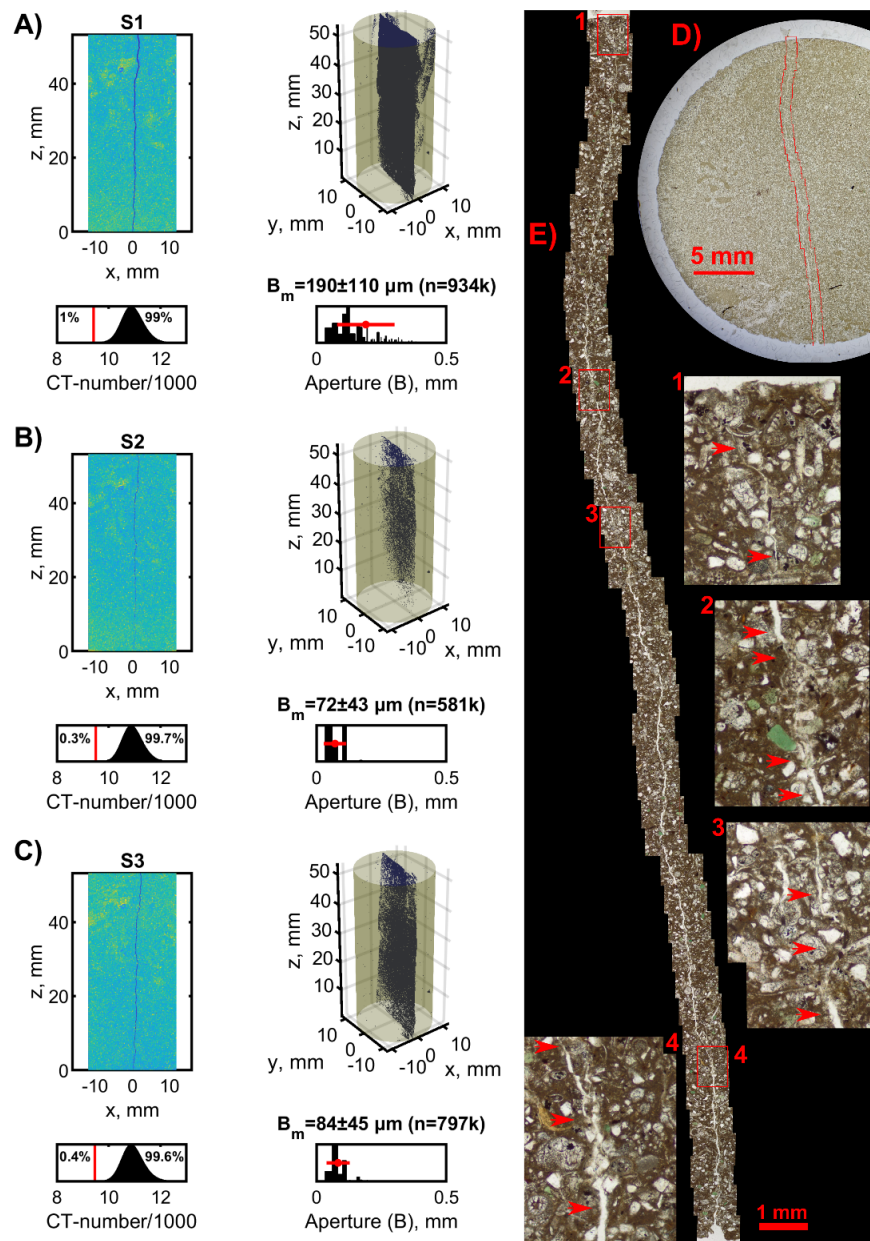
Ultrasonic velocity measurements (Fig. 2A) show that V_p and V_s increase with σ_m , and the younger samples (FB12 and GB13) generally have lower wave speeds. V_p to V_s ratios vary between 1.6 and 1.9, with the least consolidated and youngest sample (FB12) exhibiting the highest values. After saturation, sample GB13 V_p

increased by ~ 250 m/s on average while V_s decreased by ~ 100 m/s on average, increasing the V_p to V_s ratio from ~ 1.65 to ~ 1.95 .

Figure 2. A) The left-top panel reports ultrasonic velocities measured on the four dry samples as a function of mean stress (σ_M). The right-top panel shows ultrasonic V_p and V_s for sample GB13 when dry and saturated with water. The dashed line indicates the theoretical dry velocity from Gassmann fluid substitution (Gassmann, 1951), considering the dry sample velocities, density, and porosity. The inset shows examples of P and S waveforms recorded for the dry sample at the conditions indicated by the circled dots. The bottom panels report the V_p / V_s ratios for the laboratory data and the fitting curves reported in the panels above. B) Permeability for samples FB12, MT07, and MO02 as a function of effective stress (σ'). An example of pore pressure (P_p) equilibration and fitting curves (dashed lines) are shown in the "Pp equilibration" inset. During (a) sample FB12 was compacted by step increasing and by holding σ_M for several hours; an example of partial compaction is shown in the "FB12 creep" inset. The loss of porosity of sample FB12 due to compaction is shown in the inset "FB12 compaction". The blue and red curves show the permeability of sample MT07 after fracturing (S1 and Fig. 3A) and during healing in two consecutive cycles (kT1 and kT2). During kT1 (b), the sample was kept at a confining pressure of 70 MPa for more than 48 hours. kT2 was acquired ~ 30 days after cycle 1. The end of kT2 was stage S2, where the sample was CT-scanned (Fig. 3B) and exposed to a $>97\%$ relative humidity atmosphere for 72 hours, and then stage S3, where we CT-scanned (Fig. 3C) and remeasured permeability.

Before compaction, sample FB12 permeability ranged between 200 and 400 μD . Then, we raised P_c twice to 70 MPa, causing the permeability to decrease by a factor of two and porosity by 3% (i.e., at $\sigma_m \sim 7$ MPa, porosity varied from 17.3 to 14.2%). In the following two cycles, where P_c reached 200 MPa, porosity further decreased to 13.9%, and the permeability declined by almost an order of magnitude. Concurrently, the ultrasonic V_p increased from 2.6 km/s to 4 km/s.

Samples MO02 and MT07, when intact, have permeabilities below 100 nD, regardless of σ' . The permeability of the fractured MT07 evolved between stages S1, S2, and S3. After S1 and during the first permeability measurement cycle (kT1), the permeability dropped from 2 μD to 87 nD. After exposing the sample to $\sigma' \sim 65$ MPa for more than 48 hours (Fig 4B b), we performed a permeability test, and found that the permeability further decreased to 24 nD. The permeability remained ~ 2 orders of magnitude lower than the permeability at S1, i.e., around 30 nD, when σ' was reduced. The second permeability testing cycle (kT2) started 39 days after the end of kT1. The increase of σ' caused the permeability to drop to 9 nD. During the following decrease of σ' , the permeability resembled pre-fracturing values. A final test was performed at $\sigma' 4.5$ MPa and permeability dropped to 300 nD, seven times lower than the initial value measured at $\sigma' 5.6$ MPa. After exposing the sample to humidity (S3) for 72 hours, the permeability, measured at $\sigma' 3.7$ MPa, decreased from the S2 value by roughly five times.



Visual inspection of CT-scans collected at S1, S2 and S3 reveal the variation of fracture aperture. Similarly, aperture analyses confirm that B_m varied from 190 ± 110 , to 72 ± 43 and $84 \pm 45 \mu\text{m}$ during the S1, S2, and S3, respectively (Fig. 3ABC). During the same stages, the number of voxel counted within the fracture varied respectively from $\sim 934,000$ to $\sim 581,000$ and $\sim 797,000$. Microphotography of sample MT07 at stage S3, shows that in several loci, the fracture collapsed, and a fine-grained amorphous mass infilled the fracture (Fig. 3DE).

Figure 3. CT-scan and transmitted light microphotography of sample MT07 sample after fracturing. Panels A, B, and C report CT-scan data at stages S1, S2, and S3, respectively. Each top-left inset of panels A-C show x-z sections of the CT-scan model after CT-number normalization, whose distribution is shown in the inset below. The red vertical line indicates the binarization threshold, and the percentages on the left and the right of such a line indicate the relative quantity of voxels representing air and solid rock, respectively. The

right top inset in each A-C panel shows the binarized 3D model, where voxels collected within the fracture are shown in blue. The bottom right insets show the aperture distribution (B), the calculated average and standard deviation (B_m - red bars) and the total count of voxel within the fracture between parenthesis. Panel D is a microphotography of the thin section at stage S3. Panel E is a zoom of panel D highlighted in red. Insets 1 to 4 show fracture infill, which are highlighted by red arrows along with open fractures.

4 Discussion

We provide porosity-permeability relationships for rock samples from the subaerial northern HM under a range of confining pressures. Ultrasonic velocities of dry samples are similar to the seismic velocities estimated offshore New Zealand by the SHIRE project (Gase et al., 2021). The seismic reflectivity imaged along the transect MC10 shows the decollement along the prism base and several splay faults that may partly accommodate the convergence (Fig. 4A). Inside the prism, V_p increases gradually from 2.0 km/s near the surface to 4.5 km/s at the prism base ~ 7 km below sea level. A comparison between the seismic velocities in figure 4B and our ultrasonic velocities shows that samples GB13 and FB12 are representative of the modern slope basins on the outer prism, which is consistent with their depositional environment. The physical properties of sample MT07 of the Tinui Group correspond well to the velocities of the deep part of the prism, where V_p reaches 4.5 km/s. Compaction and diagenesis must contribute to the increase in V_p with depth (Dvorkin & Nur, 1996; Saxena & Mavko, 2014). We measured an ultrasonic V_p of 4.8 km/s at 150 MPa in the Torlesse basement sample MO02, which is higher than what we imaged in the deep prism on Line MC10 (Fig. 4), suggesting that there may not be a deep offshore portion of the Torlesse basement offshore northern HM (Bassett et al., 2022; Gase et al., 2021).

When comparing seismic and ultrasonic velocities, we should note that they have been estimated at frequencies around 20 Hz and 800 kHz, respectively. Considering such a frequency range, a typical P-wave quality factor range of 30 to 150, and a nearly-constant Q model (Liu et al., 1976; Tisato et al., 2021), we should expect velocities to increase between 2.3 and 12%. Another difference between SHIRE and laboratory data is that the latter are measured on dry samples, whereas the accretionary prism must be saturated. We show that P-wave velocities increase by $\sim 10\%$ when sample GB13 is saturated, suggesting that the effects of fluid saturation and anelasticity on velocities should counteract each other. Given the similarity in P-wave velocities and depositional environment, we suggest that the Tinui and Tolaga group rocks (samples MT07 and GB13) are good lithological proxies for the deep and shallow offshore Hikurangi prism, respectively.

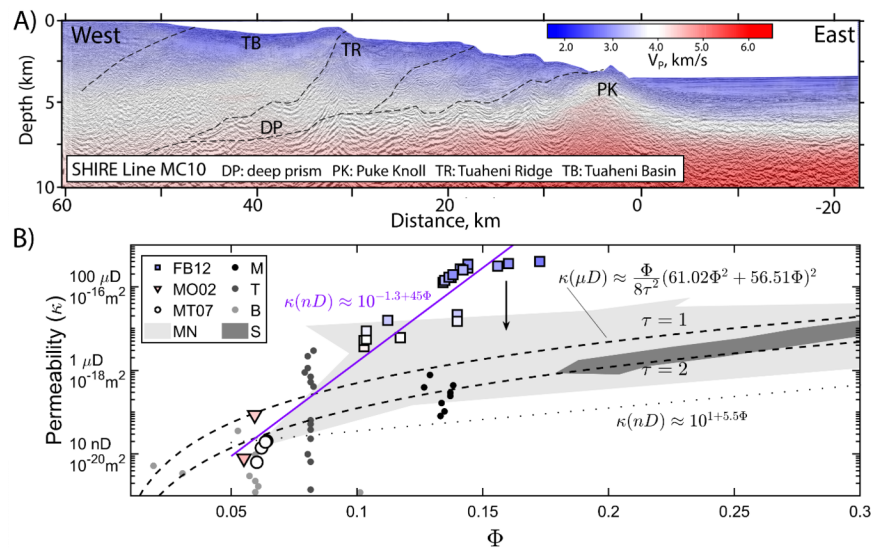


Figure 4. A) Velocity model along the SHIRE Line MC10 (Gase et al., 2021). MC10 position is reported in

figure S1. B) Summary of laboratory result: permeabilities vs porosity and color-coded markers as a function of measured ultrasonic V_p for samples FB12, MO02, and MT07. Color coding is based on the colorbar of panel A. The arrow indicates in which direction the permeabilities vary when tests are performed using water rather than helium gas. Dashed lines indicate empirical permeability vs porosity according to eq. 3. The dotted line represents an average permeability for unconsolidated clays and possibly a lower bound for the permeability of HM sediments (Neuzil, 1994). S data (dark-gray area) are for siltstones (Reece et al., 2012). The continuous line fits our data and agrees with measured mudstone permeabilities indicated by the MN gray-shaded area (Magara, 1978; Neglia, 1979). Such a line also represents an upper bound for the permeability of HM rocks. M, T, and B data are permeabilities measured in boreholes: M by Reisdorf et al. (2016), Yu et al. (2017); T by Boisson et al. (2001); B by Intera Eng. Ltd. (2011), Roberts et al. (2011), Walsh (2011).

The permeability of our samples ranges from 1 nD to 1 mD, with the samples representing the deep part of the prism being the tightest. Neuzil (1994, 2019) compiled data from several studies on unconsolidated clays with a maximum porosity of 80%, and a few consolidated mudstone-siltstones with porosities (Φ) <35%. Saffer & Bekins (1998) followed Neuzil’s work and described the permeability (κ) of the Nankai accretionary complex as:

$$\kappa \text{ (nD)} \approx 10^{1+5.5\phi} \text{ eq. 1}$$

Equation 1 fits the porosity-permeability relationship of unconsolidated sediments and is a lower bound for the permeability of mudstones that are similar to our samples (Magara, 1978; Neglia, 1979; Reece et al., 2012). On the other hand, we found that:

$$\kappa \text{ (nD)} \approx 10^{-1.3+45\phi} \text{ eq. 2}$$

fits our results and is an upper bound for the permeability of mudstones. We suggest that the permeabilities comprised between equations 1 and 2 (Fig. 4B MN,S) are proxies for rock permeabilities in the Northern Hikurangi accretionary prism at depths >1 km, because helium gas limits clay swelling, which would have lowered the measured permeabilities (Villar et al., 2005); At burial depths >1-2 km, the porosity of clay-bearing sediments, mudstones, siltstone, and shales drops below 35% (Griffiths & Joshi, 1989; Skempton, 1969; Magara, 1978); Permeabilities measured in boreholes are typically orders of magnitude higher than those measured in the laboratory due to the presence of fractures (Fig 4B lines M,T,B) (Neuzil, 2019), and numerical models of permeability in microfractured claystones agree with the mudstone porosity-permeability in fig 5B (Vora & Dugan, 2019). We also propose that the permeability of rocks in the Northern Hikurangi accretionary prism can be described by a Kozeny-Carman relation (dashed lines in Fig 4B):

$$\kappa = \frac{\phi}{8\tau^2} R^2 \text{ eq. 3}$$

Where τ is tortuosity and R is the median pore diameter (Carman, 1997). We obtained R (nm) = $61.02\phi^2 + 56.51\phi$ from data reported by Hunt (1996).

Every 1-2 years, the northern HM experiences an SSE that lasts several weeks (Wallace, 2020). Recent analyses of the APG data offshore Gisborne have shown that the 2014 SSE may have experienced up to 30 cm of slip in the center of a ~100 km wide patch, though less displacement is expected along the edges (Yohler et al., 2019). Some authors have suggested that SSEs that originate along the decollement at the base of the wedge are accompanied by slip diverted to thrust faults in the Hikurangi accretionary wedge (Shaddock & Schwartz, 2019). We expect mudstones along these thrust faults to experience fracturing during an SSE. Our laboratory measurements before and after rock failure for sample MT07 show that the deeper prism, where Tinui Group equivalent rocks may be present, may experience large increases in permeability during an SSE.

In a few weeks, the fractured sample MT07 regained its pre-fracturing permeability. Between stages S1 and S2, the permeability recovery was achieved in dry conditions. Although sample MT07 and sample FB12 have different compaction levels and grain sizes, they share a similar mineralogy. Thus, although limited, we expect plastic deformation also in sample MT07, likely concentrated near clays (Mondol et al., 2008).

Between stages S2 and S3, the permeability decreased by a factor of 5, while B_m increased, suggesting clay expansion. Once confined, we expect that the hydrated clays would deform plastically, clogging the fracture more efficiently than dry clays and justifying the observed permeability loss. We propose that such efficient permeability healing is also present along HM faults, given the presence of clays at depth, especially above the 5-7 km deep temperature-controlled smectite-illite transition (Freed & Peacor, 1989; Pecher et al., 2017; Tisato & Marelli, 2013).

In the Hikurangi subduction zone, fluids expelled from pore space and fluids released by dehydration reactions travel along the plate interface or through the accretionary wedge (Ellis et al., 2015). As the fluid pressure increases near the decollement and inside the accretionary wedge, conditions may become favorable for an SSE (Kobayashi & Sato, 2021). Though this mechanism has been proposed for several subduction zones where SSE occur at larger depths (Audet et al., 2009; Kodaira et al., 2004), the analysis of Warren-Smith et al. (2019) shows that the northern HM also can seal fluid pathways after an SSE. The expansion and plastic deformation of clays, which we have observed in our laboratory tests, may provide an efficient mechanism to reduce permeability over weeks or months after an SSE.

5 Conclusions

We provided relationships between porosity, permeability, and confining pressure for rocks that make up the accretionary prism of the northern HM. We suggest an empirical porosity-permeability relationship to model fluid transport and estimate effective stress in shallow subduction zones. Mechanical failure of these rocks enhances permeability, but over the course of several weeks, healing reduces the permeability again, suggesting that after an SSE, mudstones deep in the northern HM accretionary prism can recover permeability efficiently within the time frame of an SSE as a mechanism explaining the regular recurrence of these events.

Acknowledgments

NT thanks Luc Lavier and Dominic Strogen for the valuable discussions. NSF supported this research (grant OCE-1949171).

Open Research

Data are publicly available upon publication at <https://doi.org/10.18738/T8/RMXMIQ> or can be requested to the corresponding author.

References

- Adams, C. J., & Graham, I. J. (1996). Metamorphic and tectonic geochronology of the Torlesse Terrane, Wellington, New Zealand. *New Zealand Journal of Geology and Geophysics* , 39 (2), 157–180. <https://doi.org/10.1080/00288306.1996.9514703>
- Aretusini, S., Meneghini, F., Spagnuolo, E., Harbord, C. W., & Di Toro, G. (2021). Fluid pressurisation and earthquake propagation in the Hikurangi subduction zone. *Nature Communications* , 12 (1), 2481. <https://doi.org/10.1038/s41467-021-22805-w>
- Arp, V. D., McCarty, R. D., & Friend, D. G. (1998). *Thermophysical Properties of Helium-4 from 0.8 to 1500 K with Pressures to 2000 MPa* (Technical Report No. 1334 (revised)). NIST.
- Audet, P., Bostock, M. G., Christensen, N. I., & Peacock, S. M. (2009). Seismic evidence for overpressured subducted oceanic crust and megathrust fault sealing. *Nature* , 457 , 76–78. <https://doi.org/10.1038/nature07650>
- Barnes, P. M., Wallace, L. M., Saffer, D. M., Bell, R. E., Underwood, M. B., Fagereng, A., et al. (2020). Slow slip source characterized by lithological and geometric heterogeneity. *Science Advances* , 6 (13). <https://doi.org/10.1126/sciadv.aay3314>

- Bassett, D., Arnulf, A., Henrys, S., Barker, D., Avendonk, H., Bangs, N., et al. (2022). Crustal Structure of the Hikurangi Margin From SHIRE Seismic Data and the Relationship Between Forearc Structure and Shallow Megathrust Slip Behavior. *Geophysical Research Letters* ,49 (2). <https://doi.org/10.1029/2021GL096960>
- Bell, R., Sutherland, R., Barker, D. H. N., Henrys, S., Bannister, S., Wallace, L., & Beavan, J. (2010). Seismic reflection character of the Hikurangi subduction interface, New Zealand, in the region of repeated Gisborne slow slip events. *GJI* , 180 , 34–48. <https://doi.org/10.1111/j.1365-246X.2009.04401.x>
- Birch, F. (1960). The velocity of compressional waves in rocks to 10 kilobars: 1. *Journal of Geophysical Research* , 65 (4), 1083–1102. <https://doi.org/10.1029/JZ065i004p01083>
- Bland, K. J., Uruski, C. I., & Isaac, M. J. (2015). Pegasus Basin, eastern New Zealand: A stratigraphic record of subsidence and subduction, ancient and modern. *NZJGG* , 58 , 319–343. <https://doi.org/10.1080/00288306.2015.1076862>
- Boisson, J.-Y., Bertrand, L., Heitz, J.-F., & Golvan, Y. (2001). In situ and laboratory investigations of fluid flow through an argillaceous formation at different scales of space and time, Tournemire tunnel, southern France. *Hydrogeology Journal* , 9 (1), 108–123. <https://doi.org/10.1007/s100400000119>
- Carman, P. C. (1997). Fluid flow through granular beds. *Chemical Engineering Research and Design* , 75 , S32–S48. [https://doi.org/10.1016/S0263-8762\(97\)80003-2](https://doi.org/10.1016/S0263-8762(97)80003-2)
- Dutilleul, J., Bourlange, S., & Géraud, Y. (2021). Porosity and compaction state at the active Pāpaku thrust fault in the frontal accretionary wedge of the north Hikurangi margin. *G3* , 22 , e2020GC009325. <https://doi.org/10.1029/2020GC009325>
- Dvorkin, J., & Nur, A. (1996). Elasticity of high-porosity sandstones: Theory for two North Sea data sets. *GEOPHYSICS* , 61 (5), 1363–1370. <https://doi.org/10.1190/1.1444059>
- Ellis, S., Fagereng, Å., Barker, D., Henrys, S., Saffer, D., Wallace, L., et al. (2015). Fluid budgets along the northern Hikurangi subduction margin, New Zealand: the effect of a subducting seamount on fluid pressure. *GJI* , 202 , 277–297. <https://doi.org/10.1093/gji/ggv127>
- Fagereng, Å., Savage, H. M., Morgan, J. K., Wang, M., Meneghini, F., Barnes, P. M., et al. (2019). Mixed deformation styles observed on a shallow subduction thrust, Hikurangi margin, New Zealand. *Geology* , 47 , 872–876. <https://doi.org/10.1130/G46367.1>
- Freed, R. L., & Peacor, D. R. (1989). Variability in temperature of the smectite/illite reaction in Gulf Coast sediments. *Clay Minerals* ,24 (2), 171–180. <https://doi.org/10.1180/claymin.1989.024.2.05>
- French, M. E., & Morgan, J. K. (2020). Pore Fluid Pressures and Strength Contrasts Maintain Frontal Fault Activity, Northern Hikurangi Margin, New Zealand. *GRL* , 47 , e2020GL089209. <https://doi.org/10.1029/2020GL089209>
- Gase, A. C., Van Avendonk, H. J. A., Bangs, N. L., Bassett, D., Henrys, S. A., Barker, D. H. N., et al. (2021). Crustal Structure of the Northern Hikurangi Margin, New Zealand: Variable Accretion and Overthrusting Plate Strength Influenced by Rough Subduction. *Journal of Geophysical Research: Solid Earth* , 126 (5), e2020JB021176. <https://doi.org/10.1029/2020JB021176>
- Gassmann, F. (1951). Elastic waves through a packing of spheres. *GEOPHYSICS* , 16 (4), 673–685. <https://doi.org/10.1190/1.1437718>
- Griffiths, F. J., & Joshi, R. C. (1989). Change in pore size distribution due to consolidation of clays. *Géotechnique* ,39 (1), 159–167. <https://doi.org/10.1680/geot.1989.39.1.159>
- Hunt, J. M. (1996). *Petroleum geochemistry and geology* (2nd ed). New York: W.H. Freeman.
- Im, K., Saffer, D., Marone, C., & Avouac, J. P. (2020). Slip-rate-dependent friction as a universal mechanism for slow slip events. *Nature Geoscience* , 13 (10). <https://doi.org/10.1038/s41561-020-0627-9>

Intera Eng. Ltd. (2011). *Descriptive Geosphere Site Model* . 2011: Intera Eng. Ltd.

Kerschnitzki, M., Kollmannsberger, P., Burghammer, M., Duda, G. N., Weinkamer, R., Wagermaier, W., & Fratzl, P. (2013). Architecture of the osteocyte network correlates with bone material quality: OSTEOCYTE NETWORK ARCHITECTURE CORRELATES WITH BONE MATERIAL QUALITY. *Journal of Bone and Mineral Research* , 28 (8), 1837–1845. <https://doi.org/10.1002/jbmr.1927>

Kobayashi, T., & Sato, T. (2021). Estimating Effective Normal Stress During Slow Slip Events From Slip Velocities and Shear Stress Variations. *Geophysical Research Letters* , 48 (20). <https://doi.org/10.1029/2021GL095690>

Kodaira, S., Iidaka, T., Kato, A., Park, J.-O., Iwasaki, T., & Kaneda, Y. (2004). High pore fluid pressure may cause silent slip in the Nankai Trough. *Science* , 304 , 1295–1298.

van de Lagemaat, S. H. A., Mering, J. A., & Kamp, P. J. J. (2022). Geochemistry of syntectonic carbonate veins within Late Cretaceous turbidites, Hikurangi margin (New Zealand): Implications for a mid-Oligocene age of subduction initiation. *G3* , 23 , e2021GC010125. <https://doi.org/10.1029/2021GC010125>

Leah, H., Fagereng, Å., Bastow, I., Bell, R., Lane, V., Henrys, S., et al. (2022). The northern Hikurangi margin three-dimensional plate interface in New Zealand remains rough 100 km from the trench. *Geology* , 50 , 1256–1260. <https://doi.org/10.1130/G50272.1>

Lee, T. C., Kashyap, R. L., & Chu, C. N. (1994). Building Skeleton Models via 3-D Medial Surface Axis Thinning Algorithms. *CVGIP: Graphical Models and Image Processing* , 56 (6), 462–478. <https://doi.org/10.1006/cgip.1994.1042>

Liu, H.-P., Anderson, D. L., & Kanamori, H. (1976). Velocity dispersion due to anelasticity; implications for seismology and mantle composition. *Geophysical Journal International* , 47 (1), 41–58. <https://doi.org/10.1111/j.1365-246X.1976.tb01261.x>

Magara, K. (1978). *Compaction and fluid migration: practical petroleum geology* . Amsterdam, New York: Elsevier Scientific Pub. Co. ; Distributors for the U.S. and Can., Elsevier North-Holland.

Maurer, C. R., Rensheng Qi, & Raghavan, V. (2003). A linear time algorithm for computing exact Euclidean distance transforms of binary images in arbitrary dimensions. *IEEE Transactions on Pattern Analysis and Machine Intelligence* , 25 (2), 265–270. <https://doi.org/10.1109/TPAMI.2003.1177156>

Mavko, G., Mukerji, T., & Dvorkin, J. (2019). *The rock physics handbook* (Third edition). Cambridge, United Kingdom: Cambridge University Press.

Mazengarb, C., & Speden, I. G. (2000). Geology of the Raukumara area. geological map 6 60 p. + 1 fold. map, Lower Hutt: Institute of Geological & Nuclear Sciences.

Mondol, N. H., Bjorlykke, K., & Jahren, J. (2008). Experimental compaction of clays: relationship between permeability and petrophysical properties in mudstones. *Petroleum Geoscience* , 14 (4), 319–337. <https://doi.org/10.1144/1354-079308-773>

Mortimer, N., Rattenbury, M., King, P., Bland, K., Barrell, D., Bache, F., et al. (2014). High-level stratigraphic scheme for New Zealand rocks. *New Zealand Journal of Geology and Geophysics* , 57 (4), 402–419. <https://doi.org/10.1080/00288306.2014.946062>

Neglia, S. (1979). Migration of Fluids in Sedimentary Basins. *AAPG Bulletin* , 63 (4), 573–597. <https://doi.org/10.1306/2F918194-16CE-11D7-8645000102C1865D>

Neuzil, C. E. (1994). How permeable are clays and shales? *Water Resources Research* , 30 (2), 145–150. <https://doi.org/10.1029/93WR02930>

Neuzil, C. E. (2019). Permeability of Clays and Shales. *Annual Review of Earth and Planetary Sciences* , 47 (1), 247–273. <https://doi.org/10.1146/annurev-earth-053018-060437>

- Ortiz-Vega, D., Hall, K., Holste, J., Arp, V., Harvey, A., & Lemmon, E. (2020). Helmholtz equation of state for helium. *Journal of Physical and Chemical Reference Data* .
- Passarelli, L., Selvadurai, P. A., Rivalta, E., & Jonsson, S. (2021). The source scaling and seismic productivity of slow slip transients. *Science Advances* , 7 (32), eabg9718. <https://doi.org/10.1126/sciadv.abg9718>
- Pecher, I. A., Villinger, H., Kaul, N., Crutchley, G. J., Mountjoy, J. J., Huhn, K., et al. (2017). A Fluid Pulse on the Hikurangi Subduction Margin: Evidence From a Heat Flux Transect Across the Upper Limit of Gas Hydrate Stability. *Geophysical Research Letters* , 44 (24). <https://doi.org/10.1002/2017GL076368>
- Prelicz, R. M. (2005). *Seismic anisotropy in peridotites from the Western Gneiss Region (Norway): laboratory measurements at high PT conditions and fabric based model predictions* [Application/pdf]. ETH Zurich. <https://doi.org/10.3929/ETHZ-A-005115293>
- Rabinowitz, H. S., Savage, H. M., Skarbek, R. M., Ikari, M. J., Carpenter, B. M., & Collettini, C. (2018). Frictional behavior of input sediments to the Hikurangi trench, New Zealand. *G3* , 19 , 2973–2990. <https://doi.org/10.1029/2018GC007633>
- Reece, J. S., Flemings, P. B., Dugan, B., Long, H., & Germaine, J. T. (2012). Permeability-porosity relationships of shallow mudstones in the Ursa Basin, northern deepwater Gulf of Mexico: MUDSTONE PERMEABILITY-POROSITY BEHAVIOR. *Journal of Geophysical Research: Solid Earth* , 117 (B12), n/a-n/a. <https://doi.org/10.1029/2012JB009438>
- Reisdorf, A. G., Hostettler, B., Jaeggi, D., Deplazes, G., Blaesi, H., Morard, A., et al. (2016). Litho- and biostratigraphy of the 250 m-deep Mont Terri BDB-1 borehole through the Opalinus Clay and bounding formations, St Ursanne, Switzerland. <https://doi.org/10.13140/RG.2.2.15045.04322>
- Roberts, R., Chace, D., Beauheim, R., & Avis, J. (2011). *Analysis of straddle-packer tests in DGR boreholes* (Technical report No. TR-08-32). Ottawa, Canada: Geofirma Eng. Ltd.
- Saffer, D. M., & Bekins, B. A. (1998). Episodic fluid flow in the Nankai accretionary complex: Timescale, geochemistry, flow rates, and fluid budget. *Journal of Geophysical Research: Solid Earth* , 103 (B12), 30351–30370. <https://doi.org/10.1029/98JB01983>
- Saffer, D. M., & Wallace, L. M. (2015). The frictional, hydrologic, metamorphic and thermal habitat of shallow slow earthquakes. *NG* , 8 , 594–600. <https://doi.org/10.1038/ngeo2490>
- Saxena, N., & Mavko, G. (2014). Exact equations for fluid and solid substitution. *GEOPHYSICS* , 79 (3), L21–L32. <https://doi.org/10.1190/geo2013-0187.1>
- Schwartz, S. Y., & Rokosky, J. M. (2007). Slow slip events and seismic tremor at circum-Pacific subduction zones. *RG* , 45 , RG3004. <https://doi.org/10.1029/2006RG000208>
- Shaddock, H. R., & Schwartz, S. Y. (2019). Subducted seamount diverts shallow slow slip to the forearc of the northern Hikurangi subduction zone, New Zealand. *Geology* , 47 , 415–418. <https://doi.org/10.1130/G45810.1>
- Shreedharan, S., Ikari, M., Wood, C., Saffer, D., Wallace, L., & Marone, C. (2022). Frictional and Lithological Controls on Shallow Slow Slip at the Northern Hikurangi Margin. *G3* , 23 , e2021GC010107. <https://doi.org/10.1029/2021GC010107>
- Skempton, A. W. (1969). The consolidation of clays by gravitational compaction. *Quarterly Journal of the Geological Society* , 125 (1–4), 373–411. <https://doi.org/10.1144/gsjgs.125.1.0373>
- Sun, T., Saffer, D., & Ellis, S. (2020). Mechanical and hydrological effects of seamount subduction on megathrust stress and slip. *Nature Geoscience* , 13 (3), 249–255. <https://doi.org/10.1038/s41561-020-0542-0>
- Sutherland, H. J., & Cave, S. P. (1980). Argon gas permeability of new mexico rock salt under hydrostatic compression. *International Journal of Rock Mechanics and Mining Sciences & Geomechanics Abstracts* , 17

(5), 281–288. [https://doi.org/10.1016/0148-9062\(80\)90810-4](https://doi.org/10.1016/0148-9062(80)90810-4)

Tisato, N., & Marelli, S. (2013). Laboratory measurements of the longitudinal and transverse wave velocities of compacted bentonite as a function of water content, temperature, and confining pressure: ELASTIC PROPERTIES OF BENTONITE. *Journal of Geophysical Research: Solid Earth* , 118 (7), 3380–3393. <https://doi.org/10.1002/jgrb.50252>

Tisato, N., Madonna, C., & Saenger, E. H. (2021). Attenuation of Seismic Waves in Partially Saturated Berea Sandstone as a Function of Frequency and Confining Pressure. *Frontiers in Earth Science* , 9 , 641177. <https://doi.org/10.3389/feart.2021.641177>

Villar, M. V., Martin, P. L., & Barcala, J. M. (2005). Modification of physical, mechanical and hydraulic properties of bentonite by thermo-hydraulic gradients. *Engineering Geology* , 81 (3), 284–297. <https://doi.org/10.1016/j.enggeo.2005.06.012>

Vora, H. B., & Dugan, B. (2019). Porosity-Permeability Relationships in Mudstone from Pore-Scale Fluid Flow Simulations using the Lattice Boltzmann Method. *Water Resources Research* , 55 (8), 7060–7071. <https://doi.org/10.1029/2019WR024985>

Wallace, Laura M. (2020). Slow Slip Events in New Zealand. *AREPS* , 48 , 175–203. <https://doi.org/10.1146/annurev-earth-0717190055104>

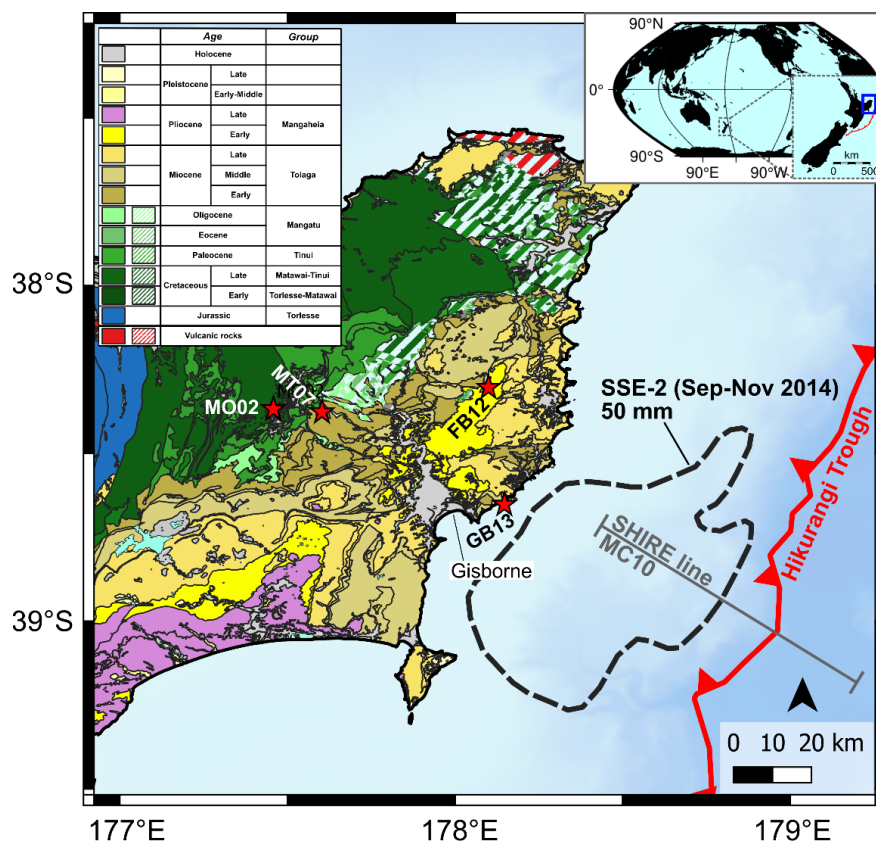
Wallace, L.M., Saffer, D. M., Barnes, P. M., Pecher, I. A., Petronotis, K. E., LeVay, L. J., & the Expedition 372/375 Scientists. (2019). *Hikurangi Subduction Margin Coring, Logging, and Observatories* . College Station, TX: Proceedings of the International Ocean Discovery Program, 372B/375. <https://doi.org/10.14379/iodp.proc.372B375.102.2019>

Walsh, R. (2011). *Compilation and consolidation of field and laboratory data for hydrogeological properties* (DGR Site Charact. Doc. No. TR-08-10). Ottawa, Canada: Geofirma Eng. Ltd.

Warren-Smith, E., Fry, B., Wallace, L., Chon, E., Henrys, S., Sheehan, A., et al. (2019). Episodic stress and fluid pressure cycling in subducting oceanic crust during slow slip. *Nature Geoscience* , 12 (6), 475–481. <https://doi.org/10.1038/s41561-019-0367-x>

Yohler, R., Bartlow, N., Wallace, L. M., & Williams, C. (2019). Time-Dependent Behavior of a Near-Trench Slow-Slip Event at the Hikurangi Subduction Zone. *Geochemistry, Geophysics, Geosystems* , 20 (8), 4292–4304. <https://doi.org/10.1029/2019GC008229>

Yu, C., Matray, J.-M., Goncalves, J., Jaeggi, D., Grasle, W., Wiczeorek, K., et al. (2017). Comparative study of methods to estimate hydraulic parameters in the hydraulically undisturbed Opalinus Clay (Switzerland). *Swiss Journal of Geosciences* , 110 (1), 85–104. <https://doi.org/10.1007/s00015-016-0257-9>



Supporting Information

Figure S1. Geologic map of the Raukumara peninsula with the position of the rock samples used in this study (Mazengarb & Speden, 2000). The offshore dashed line contours marks the 50 mm geodetic slip model for the September–November 2014 SSE (Warren-Smith et al., 2019). The offshore line indicates the seismic line MC10 from the SHIRE project (Gase et al., 2021).

Sample preparation details

The end faces of each core plug were smoothed to parallel using a rock saw and a lathe equipped with an angular grinder. Parallelism was checked with a 0.01 mm resolution caliper. Each core was oven-dried at ~333 K for several days to reduce absorbed water. We then calculated the total volume and density of each core by measuring its mass and dimensions using a scale and a caliper to accuracies of 0.001 g and 0.02 mm, respectively. A helium pycnometer (Micromeritics AccuPyc II 1340) was used to measure the solid volume and porosity of each core.

To evenly distribute the saturating water or the helium gas to test permeability across the sample end-face, we placed 3.175 mm thickness, 10 μ m grain size, AISI 316 stainless steel porous frits between each sample holder and the adjacent sample end-face.

Sample MT07 at stage S3 - i.e., fractured after being exposed to humidity - was epoxy impregnated before removing the rubber jacket to avoid offsetting the fracture.

Preparation of the saturating water for sample GB13

Water chemically equilibrated with sample GB13 was prepared and injected as follows: For several weeks before saturation, we submerged a few grams of GB13 granules in deionized water. Then, the injection

of such aqueous fluid was performed using a high-pressure syringe pump (ISCO 260HP), recording – via a Matlab script - the injected volume and injection pressure. The latter was maintained constant to a value of 3 MPa lower than the confining pressure that varied between 20 and 50 MPa.

Ultrasonic and mechanical testing details

Our samples have a maximum ultrasonic velocity of ~ 6 km/s and considering the testing frequency of 800 kHz, we estimated a maximum wavelength (λ_M) of 7.5 mm and, to avoid nearfield effects, we prepared cores with a length (L) $> 3 \lambda_M$. Velocities were estimated with the transmission method by measuring the time of travel of the elastic wave along the core plug (Birch, 1960). We corrected the first arrival by the delay introduced by the sample holders that was determined by a standard calibration procedure (e.g., Prelicz, 2005). A pulser-receiver apparatus (JSR Ultrasonics DPR300) generated a negative spike pulse with a typical duration of ~ 40 ns feeding the source ultrasonic transducer. We used a pulsing rate of 100 pulses/sec (PRF RATE=1), pulse amplitude of ~ 194 V (PULSE AMPLITUDE = 4, and PULSE ENERGY = HIGH Z 4), and damping of 331 Ohms (DAMPING = 1). In addition, the pulser-receiver produces a trigger signal (5 V in amplitude) to synchronize the pulser and the oscilloscope (Rigol DS1104Z-S) collecting the signals generated by the receiving transducer and amplified by the receiver. The latter has a gain of 66 dB (REL. GAIN = 79), a high-pass filter corner frequency of 1 MHz, and a low-pass filter corner frequency of 3 MHz. Two data transfer switches allow selecting the recording of the V_P , V_{S1} or V_{S2} signal. To improve the signal-to-noise ratio the oscilloscope collects and stacks 1024 signals and transmits the digitized wavelets to a computer via a USB port. Typically, the signal, comprising 1200 samples, is digitized every 0.2 μ s or less and saved as a comma-separated-value (CSV) file.

Samples compaction was measured to 1 μ m accuracy with a Linear Variable Displacement Transducer connected to the axial piston, whose signal was acquired along with the confining pressure and vertical force.

Permeability testing

The two reservoirs connected to the sample end-faces have volumes $V_1=58.725$ ml and $V_2=162.53$ ml, and at the beginning of the test, we connected the reservoirs to a high-pressure helium gas bottle to raise their internal pressures to two different values $P_{1i} > P_{2i}$. While P_{1i} is greater than P_{2i} , helium flows through the sample until pressure equilibrium is reached. Two digital manometers (Keller LEO3) connected to a computer and a Matlab code record P_1 and P_2 over time (t). The two manometers also measure temperature (T). Permeability is then calculated as:

$$\kappa = -\frac{\beta \eta L}{A}$$

$$\text{english} \left(\frac{1}{V_1} + \frac{1}{V_2} \right) K A, \text{ eq. S1}$$

Where η and K are Helium viscosity and bulk modulus, respectively; L and A are the lengths and cross-section area of the sample; β is the exponent of the pressure decay:

$$P_1 = (P_{1i} - P_{2i}) e^{\beta \tau} + P_f, \text{ eq. S2}$$

Όπου P_f κ η L A V_1 V_2 β τ P_{1i} P_{2i} P_f τ P_1 P_2 t V_1 V_2 K A L η β τ P_{1i} P_{2i} P_f τ P_1 P_2 t V_1 V_2 K A L η β τ P_{1i} P_{2i} P_f τ P_1 P_2 t V_1 V_2 K A L η β τ P_{1i} P_{2i} P_f τ P_1 P_2 t V_1 V_2 K A L η β τ P_{1i} P_{2i} P_f τ P_1 P_2 t V_1 V_2 K A L η β τ P_{1i} P_{2i} P_f τ P_1 P_2 t V_1 V_2 K A L η β τ P_{1i} P_{2i} P_f τ P_1 P_2 t V_1 V_2 K A L η β τ P_{1i} P_{2i} P_f τ P_1 P_2 t V_1 V_2 K A L η β τ P_{1i} P_{2i} P_f τ P_1 P_2 t V_1 V_2 K A L η β τ P_{1i} P_{2i} P_f τ P_1 P_2 t V_1 V_2 K A L η β τ P_{1i} P_{2i} P_f τ P_1 P_2 t V_1 V_2 K A L η β τ P_{1i} P_{2i} P_f τ P_1 P_2 t V_1 V_2 K A L η β τ P_{1i} P_{2i} P_f τ P_1 P_2 t V_1 V_2 K A L η β τ P_{1i} P_{2i} P_f τ P_1 P_2 t V_1 V_2 K A L η β τ P_{1i} P_{2i} P_f τ P_1 P_2 t V_1 V_2 K A L η β τ P_{1i} P_{2i} P_f τ P_1 P_2 t V_1 V_2 K A L η β τ P_{1i} P_{2i} P_f τ P_1 P_2 t V_1 V_2 K A L η β τ P_{1i} P_{2i} P_f τ P_1 P_2 t V_1 V_2 K A L η β τ P_{1i} P_{2i} P_f τ P_1 P_2 t V_1 V_2 K A L η β τ P_{1i} P_{2i} P_f τ P_1 P_2 t V_1 V_2 K A L η β τ P_{1i} P_{2i} P_f τ P_1 P_2 t V_1 V_2 K A L η β τ P_{1i} P_{2i} P_f τ P_1 P_2 t V_1 V_2 K A L η β τ P_{1i} P_{2i} P_f τ P_1 P_2 t V_1 V_2 K A L η β τ P_{1i} P_{2i} P_f τ P_1 P_2 t V_1 V_2 K A L η β τ P_{1i} P_{2i} P_f τ P_1 P_2 t V_1 V_2 K A L η β τ P_{1i} P_{2i} P_f τ P_1 P_2 t V_1 V_2 K A L η β τ P_{1i} P_{2i} P_f τ P_1 P_2 t V_1 V_2 K A L η β τ P_{1i} P_{2i} P_f τ P_1 P_2 t V_1 V_2 K A L η β τ P_{1i} P_{2i} P_f τ P_1 P_2 t V_1 V_2 K A L η β τ P_{1i} P_{2i} P_f τ P_1 P_2 t V_1 V_2 K A L η β τ P_{1i} P_{2i} P_f τ P_1 P_2 t V_1 V_2 K A L η β τ P_{1i} P_{2i} P_f τ P_1 P_2 t V_1 V_2 K A L η β τ P_{1i} P_{2i} P_f τ P_1 P_2 t V_1 V_2 K A L η β τ P_{1i} P_{2i} P_f τ P_1 P_2 t V_1 V_2 K A L η β τ P_{1i} P_{2i} P_f τ P_1 P_2 t V_1 V_2 K A L η β τ P_{1i} P_{2i} P_f τ P_1 P_2 t V_1 V_2 K A L η β τ P_{1i} P_{2i} P_f τ P_1 P_2 t V_1 V_2 K A L η β τ P_{1i} P_{2i} P_f τ P_1 P_2 t V_1 V_2 K A L η β τ P_{1i} P_{2i} P_f τ P_1 P_2 t V_1 V_2 K A L η β τ P_{1i} P_{2i} P_f τ P_1 P_2 t V_1 V_2 K A L η β τ P_{1i} P_{2i} P_f τ P_1 P_2 t V_1 V_2 K A L η β τ P_{1i} P_{2i} P_f τ P_1 P_2 t V_1 V_2 K A L η β τ P_{1i} P_{2i} P_f τ P_1 P_2 t V_1 V_2 K A L η β τ P_{1i} P_{2i} P_f τ P_1 P_2 t V_1 V_2 K A L η β τ P_{1i} P_{2i} P_f τ P_1 P_2 t V_1 V_2 K A L η β τ P_{1i} P_{2i} P_f τ P_1 P_2 t V_1 V_2 K A L η β τ P_{1i} P_{2i} P_f τ P_1 P_2 t V_1 V_2 K A L η β τ P_{1i} P_{2i} P_f τ P_1 P_2 t V_1 V_2 K A L η β τ P_{1i} P_{2i} P_f τ P_1 P_2 t V_1 V_2 K A L η β τ P_{1i} P_{2i} P_f τ P_1 P_2 t V_1 V_2 K A L η β τ P_{1i} P_{2i} P_f τ P_1 P_2 t V_1 V_2 K A L η β τ P_{1i} P_{2i} P_f τ P_1 P_2 t V_1 V_2 K A L η β τ P_{1i} P_{2i} P_f τ P_1 P_2 t V_1 V_2 K A L η β τ P_{1i} P_{2i} P_f τ P_1 P_2 t V_1 V_2 K A L η β τ P_{1i} P_{2i} P_f τ P_1 P_2 t V_1 V_2 K A L η β τ P_{1i} P_{2i} P_f τ P_1 P_2 t V_1 V_2 K A L η β τ P_{1i} P_{2i} P_f τ P_1 P_2 t V_1 V_2 K A L η β τ P_{1i} P_{2i} P_f τ P_1 P_2 t V_1 V_2 K A L η β τ P_{1i} P_{2i} P_f τ P_1 P_2 t V_1 V_2 K A L η β τ P_{1i} P_{2i} P_f τ P_1 P_2 t V_1 V_2 K A L η β τ P_{1i} P_{2i} P_f τ P_1 P_2 t V_1 V_2 K A L η β τ P_{1i} P_{2i} P_f τ P_1 P_2 t V_1 V_2 K A L η β τ P_{1i} P_{2i} P_f τ P_1 P_2 t V_1 V_2 K A L η β τ P_{1i} P_{2i} P_f τ P_1 P_2 t V_1 V_2 K A L η β τ P_{1i} P_{2i} P_f τ P_1 P_2 t V_1 V_2 K A L η β τ P_{1i} P_{2i} P_f τ P_1 P_2 t V_1 V_2 K A L η β τ P_{1i} P_{2i} P_f τ P_1 P_2 t V_1 V_2 K A L η β τ P_{1i} P_{2i} P_f τ P_1 P_2 t V_1 V_2 K A L η β τ P_{1i} P_{2i} P_f τ P_1 P_2 t V_1 V_2 K A L η β τ P_{1i} P_{2i} P_f τ P_1 P_2 t V_1 V_2 K A L η β τ P_{1i} P_{2i} P_f τ P_1 P_2 t V_1 V_2 K A L η β τ P_{1i} P_{2i} P_f τ P_1 P_2 t V_1 V_2 K A L η β τ P_{1i} P_{2i} P_f τ P_1 P_2 t V_1 V_2 K A L η β τ P_{1i} P_{2i} P_f τ P_1 P_2 t V_1 V_2 K A L η β τ P_{1i} P_{2i} P_f τ P_1 P_2 t V_1 V_2 K A L η β τ P_{1i} P_{2i} P_f τ P_1 P_2 t V_1 V_2 K A L η β τ P_{1i} P_{2i} P_f τ P_1 P_2 t V_1 V_2 K A L η β τ P_{1i} P_{2i} P_f τ P_1 P_2 t V_1 V_2 K A L η β τ P_{1i} P_{2i} P_f τ P_1 P_2 t V_1 V_2 K A L η β τ P_{1i} P_{2i} P_f τ P_1 P_2 t V_1 V_2 K A L η β τ P_{1i} P_{2i} P_f τ P_1 P_2 t V_1 V_2 K A L η β τ P_{1i} P_{2i} P_f τ P_1 P_2 t V_1 V_2 K A L η β τ P_{1i} P_{2i} P_f τ P_1 P_2 t V_1 V_2 K A L η β τ P_{1i} P_{2i} P_f τ P_1 P_2 t V_1 V_2 K A L η β τ P_{1i} P_{2i} P_f τ P_1 P_2 t V_1 V_2 K A L η β τ P_{1i} P_{2i} P_f τ P_1 P_2 t V_1 V_2 K A L η β τ P_{1i} P_{2i} P_f τ P_1 P_2 t V_1 V_2 K A L η β τ P_{1i} P_{2i} P_f τ P_1 P_2 t V_1 V_2 K A L η β τ P_{1i} P_{2i} P_f τ P_1 P_2 t V_1 V_2 K A L η β τ P_{1i} P_{2i} P_f τ P_1 P_2 t V_1 V_2 K A L η β τ P_{1i} P_{2i} P_f τ P_1 P_2 t V_1 V_2 K A L η β τ P_{1i} P_{2i} P_f τ P_1 P_2 t V_1 V_2 K A L η β τ P_{1i} P_{2i} P_f τ P_1 P_2 t V_1 V_2 K A L η β τ P_{1i} P_{2i} P_f τ P_1 P_2 t V_1 V_2 K A L η β τ P_{1i} P_{2i} P_f τ P_1 P_2 t V_1 V_2 K A L η β τ P_{1i} P_{2i} P_f τ P_1 P_2 t V_1 V_2 K A L η β τ P_{1i} P_{2i} P_f τ P_1 P_2 t V_1 V_2 K A L η β τ P_{1i} P_{2i} P_f τ P_1 P_2 t V_1 V_2 K A L η β τ P_{1i} P_{2i} P_f τ P_1 P_2 t V_1 V_2 K

πΦ γαιν, ανδ της 1800 προθεστιονς ωερε ζολλεστεδ ατ 1 φπς ανδ 1ξ1 βιννινγ. Τηε σουρσε-το-οβθθεστ διστανξε ωας 150.566 μμ, ανδ της σουρσε το δετεετορ 963.799 μμ. Ωε περφορμεδ α ζοντινουοε “Τ σσαν βψ αεραγινγ 2 φραμεε ανδ βψ σχιππινγ 0 φραμεε. Ωε αππλιεδ α βεαμ-ηαρδερινγ ζορρεετιον οφ 0.25 ανδ α ποστ-ρεζονοτρυετιον ρινγ ζορρεετιον υοινγ τηε φολλοωινγ παραμετερεε: οεροσαμπλε = 2, ραδιαλ βιν ωιδτη = 21, σεετορεε = 32, μινιμου αρεε λενγτη = 2, ανγυλαρ βιν ωιδτη = 9, ανγυλαρ σρεεερινγ φαετορ = 4. Τηε φιναλ ρεζονοτρυετεδ ολυμε ηαδ α οξελ οιζε οφ 33.3 μm and 1873 slices.

Fracture aperture calculation

To normalize CT-scan datasets, we fit a Gaussian function to the distribution of CT numbers to obtain a CT-number mean (m_x) and standard deviation (s_x), where x is either S1, S2, or S3. To compare datasets acquired at different stages, we shifted the CT-numbers of datasets S2 and S3 by $m_{S1} - m_{S2}$ and $m_{S1} - m_{S3}$, respectively. We added a value of 1 to each voxel, cropped each image to 718x718 pixels around the sample center, and assigned a value of 0 to pixels with a distance $>718/2$ from the sample center. We binarized the datasets to assign each voxel to either solid rock or air by applying a threshold calculated as $t_x = m_x - 2.5s_x$. Voxels with CT-number equal to or greater than t_x were assumed to represent rock and assigned a value of 255. Voxels with CT-number lower than t_x and greater than zero were assumed to be air and assigned a value of 128.

To obtain a FADP of a binarized dataset, we calculated: 1) The Euclidian distance of each voxel in the fracture. This is achieved by a) performing an iterative image morphological erosion assigning approximated distances of each fracture voxel from the fracture rim; and b) calculating the Euclidian distance of each voxel within the fracture from the closest voxel representing rock; 2) The skeleton of the fracture (SK) consisting in the voxels that are within the fracture and report the maximum Euclidian distance from the fracture rim into respect the 26 surrounding voxels. Such a device extracts the center surface while preserving the topology and Euler number, also known as the Euler characteristic of the objects (Kerschnitzki et al., 2013; Lee et al., 1994). Finally, the FADP was calculated at each SK location by doubling the Euclidian distance recorded in such voxels.

References

- Arp, V. D., McCarty, R. D., & Friend, D. G. (1998). *Thermophysical Properties of Helium-4 from 0.8 to 1500 K with Pressures to 2000 MPa* (Technical Report No. 1334 (revised)). NIST.
- Birch, F. (1960). The velocity of compressional waves in rocks to 10 kilobars: 1. *Journal of Geophysical Research*, 65 (4), 1083–1102. <https://doi.org/10.1029/JZ065i004p01083>
- Gase, A. C., Van Avendonk, H. J. A., Bangs, N. L., Bassett, D., Henrys, S. A., Barker, D. H. N., et al. (2021). Crustal Structure of the Northern Hikurangi Margin, New Zealand: Variable Accretion and Overthrusting Plate Strength Influenced by Rough Subduction. *Journal of Geophysical Research: Solid Earth*, 126 (5), e2020JB021176. <https://doi.org/10.1029/2020JB021176>
- Kerschnitzki, M., Kollmannsberger, P., Burghammer, M., Duda, G. N., Weinkamer, R., Wagermaier, W., & Fratzl, P. (2013). Architecture of the osteocyte network correlates with bone material quality: OSTEOCYTE NETWORK ARCHITECTURE CORRELATES WITH BONE MATERIAL QUALITY. *Journal of Bone and Mineral Research*, 28 (8), 1837–1845. <https://doi.org/10.1002/jbmr.1927>
- Lee, T. C., Kashyap, R. L., & Chu, C. N. (1994). Building Skeleton Models via 3-D Medial Surface Axis Thinning Algorithms. *CVGIP: Graphical Models and Image Processing*, 56 (6), 462–478. <https://doi.org/10.1006/cgip.1994.1042>
- Mazengarb, C., & Speden, I. G. (2000). Geology of the Raukumara area. geological map 6 60 p. + 1 fold. map, Lower Hutt: Institute of Geological & Nuclear Sciences.
- Ortiz-Vega, D., Hall, K., Holste, J., Arp, V., Harvey, A., & Lemmon, E. (2020). Helmholtz equation of state for helium. *Journal of Physical and Chemical Reference Data*.

Prelicz, R. M. (2005). *Seismic anisotropy in peridotites from the Western Gneiss Region (Norway): laboratory measurements at high PT conditions and fabric based model predictions* [Application/pdf]. ETH Zurich. <https://doi.org/10.3929/ETHZ-A-005115293>

Warren-Smith, E., Fry, B., Wallace, L., Chon, E., Henrys, S., Sheehan, A., et al. (2019). Episodic stress and fluid pressure cycling in subducting oceanic crust during slow slip. *Nature Geoscience*, 12 (6), 475–481. <https://doi.org/10.1038/s41561-019-0367-x>